UNITED NATIONS EDUCATIONAL, SCIENTIFIC AND CULTURAL ORGANIZATION
INTERNATIONAL ATOMIC ENERGY AGENCY
INTERNATIONAL CENTRE FOR THEORETICAL PHYSICS

SMR/917 - 5

SECOND WORKSHOP ON
SCIENCE AND TECHNOLOGY OF THIN FILMS

(11 - 29 March 1996)

Reading material about:
" Nanomechanical properties of thin films "

presented by:

R. WIESENDANGER
Universität Hamburg
Institut für Angewandte Physik
Jungiusstrasse 11
D-20355 Hamburg
Germany

These are preliminary lecture notes, intended only for distribution to participants.

Appl. Phys. A 61, 525–533 (1995)

Applied Physics A Materials Science & Processing

© Springer-Verlag 1995

Anisotropy of sliding friction on the triglycine sulfate (010) surface

H. Bluhm[1], U.D. Schwarz[1], K.-P. Meyer[2], R. Wiesendanger[1]

[1] Institute of Applied Physics, University of Hamburg, Jungiusstrasse 11, D-20355 Hamburg, Germany (Fax: + 49-40/4123-6368)
[2] Max Planck Institute of Microstructure Physics, Weinberg 2, D-06120 Halle (Saale), Germany

Received: 11 April 1995/Accepted: 18 July 1995

Abstract. The frictional properties of freshly cleaved (010) surfaces of the ferroelectric TriGlycine Sulfate (TGS) were investigated by combined scanning and friction force microscopy under ambient conditions. A frictional contrast could be observed between domains with different electrical polarity, as well as between terraces inside individual domains which are separated by steps of half of the unit-cell height or an odd multiple of this value. The latter contrast mechanism originates from the arrangement of the molecules at the surface which is chemically homogeneous, but structurally rotated by 180° between different terraces. The resulting asymmetric surface potential gives rise to a frictional anisotropy in different directions that can be detected by the force microscope, as well as to a change of the frictional force between forward and backward scan direction.

PACS: 61.16.Ch; 62.20.-x; 68.35.Bs

The friction of solids is, due to its technical relevance, one of the topics of research since the days of Amontons and Coulomb. Until recently, most of the studies have focused on macroscopic frictional phenomena which are governed by the effects of wear, plastic deformations, boundary lubrication, surface topography and surface asperities. In recent years, however, the development of new experimental tools such as the surface force apparatus [1] or the friction force microscope [2] enabled the investigation of wearless friction on molecularly or even atomically smooth surfaces, thus providing information about the microscopic (or even "nanoscopic") origins of friction.

On the theoretical side, Tomlinson [3] already recognized a long time ago that in the ideal case of two single-crystalline, atomically flat and defect-free solids, which are moved relative to each other in the absence of wear, plastic deformation and surface contamination, the only source of friction should be the interaction potential at the contact interface. Since these days, many models for wearless friction were proposed [4–10], but all of them keep the idea that the interaction potential determines the friction. This already includes implicitly that, since the surface potential of a crystal is basically determined by the species and the arrangement of the atoms at its surface, the magnitude of the frictional forces should be anisotropic and thus depend on the crystallographic directions in which the two crystals are moved relative to each other.

Despite the fact that frictional anisotropy is also predicted by molecular dynamics simulations [11–13] and can already be seen in some more macroscopic experiments [14–16], there are only very few reports about the observation of frictional anisotropy with experimental setups enabling the study of wearless friction [17, 18]. In these experiments, the friction in a certain crystallographic direction [uvw] was always the same as in the negative [$\bar{u}\bar{v}\bar{w}$] direction; variations in the frictional force were only observed if the sliding direction of the friction probe was changed by a certain angle other than 180° relative to the [uvw] -direction. This behaviour, i.e., variations in the frictional force when changing the sliding direction by angles other than 180°, will be referred to as *frictional anisotropy* in the following since up to now it was mostly used in this sense in the literature.

In this paper, however, it will be shown by means of combined scanning and friction force microscopy measurements at TriGlycine Sulfate (TGS) single-crystal cleavage faces that in the case of wearless friction on the molecular scale not only frictional anisotropy can be observed, but also a change in the frictional force when changing the sliding direction of the friction probe by 180°, i.e., moving the probe in backward direction. This behaviour will be called *directional dependence* of friction in order to separate it from the frictional anisotropy as defined above. In addition, it will be argued that the reason for this behaviour lies most probably in the asymmetry of the surface potential of the TGS (010) cleavage face.

1 Experimental

The TGS single crystal was grown from aqueous solution at a constant temperature above the Curie point

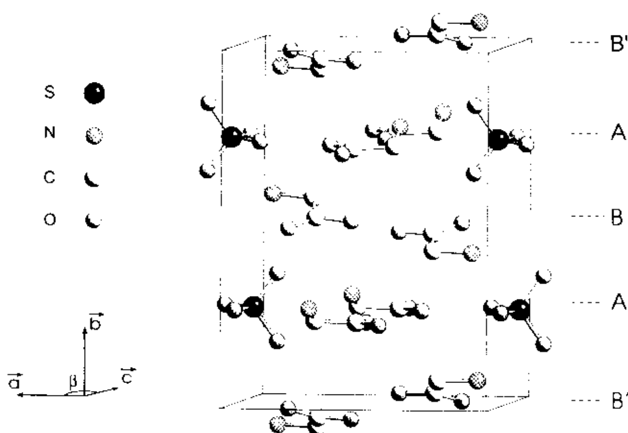

Fig. 1. Crystal structure of TGS. Hydrogen atoms are neglected. TGS can be considered to consist of layers stacked along the *b*-axis. Layers A and A' as well as B and B' are chemically equivalent, but rotated by 180° around the *b*-axis against each other, respectively

(T_c = 49 °C). The crystal structure of TGS in the ferroelectric phase can be described by the monoclinic space group $P2_1$. The lattice constants are a = 9.15 Å, b = 12.69 Å, c = 5.73 Å and β = 105° 40′ [19] (Fig. 1). The orientation of the unit-cell directions relative to the sample edges of our crystal was determined by means of X-ray diffraction using the oscillation method [20].

TGS can easily be cleaved parallel to the (010) plane. For each measurement, fresh (010) surfaces were prepared by cleaving the crystal with a razor blade in slices of about 1 mm thickness.

The combined Scanning Force Microscopy (SFM) and Friction Force Microscopy (FFM) investigations were carried out immediately after sample preparation. A commercially available SFM [21] was used which is able to monitor sample topography and frictional forces simultaneously [22, 23]. The instrument was operated in contact mode under ambient conditions. The V-shaped silicon nitride cantilevers with integrated pyramidal tips [21] had force constants of about 0.06 N/m and were scanned under an angle of 90° to their long axis at loadings between 10–100 nN. These relatively high loading forces were difficult to be further reduced and may originate in the hygroscopic nature of TGS [24], the low aspect ratio and the often truncated ends of the pyramidal tips [25] which lead to strong capillary forces on the tip.

Since the V-shaped cantilevers are difficult to calibrate correctly for absolute lateral force measurements [26], the frictional data will only be given in relative units throughout this paper. For a detailed discussion of the FFM principle see, for instance, [27].

2 Results and discussion

Figure 2a shows a topographical image of the (010) surface of TGS. Cleavage steps with heights between 1.2 and 5 nm are aligned almost perpendicular to the *a*-axis. On the flat terraces, round and irregularly shaped islands as well as holes are visible. This heterogeneous morphology is attributed to the etching of the TGS by the thin water film present at the surface [24] and the subsequent recrystallization of the etched material at the surface. The erosion of TGS by polar etchants like water was already reported in several works [28].

Figure 2b gives the FFM image of the same surface spot as shown in Fig. 2a. Two main areas differing in their frictional properties can be distinguished. A broad bright band (marked by "B" in Fig. 2b) is embedded in a darker surrounding area ("A"). Additionally, a frictional contrast within the areas "A" and "B" occurs. Comparison of Figs. 2a and b reveals that the region "A" comprises only round islands which show a brighter frictional contrast than the terrace underneath. On the other hand, area "B" contains irregularly shaped islands and holes also differing in their frictional behaviour from the surrounding terrace.

Nakatani [29] reported on the different etching behaviour of the domains with different sign of polarisation. Positive domains show a high density of etch holes, whereas the surface of negative domains is almost free of them and exhibits round islands from recrystallization processes. Haefke et al. [30] already used this characteristic property of the TGS (010) surface to denominate the

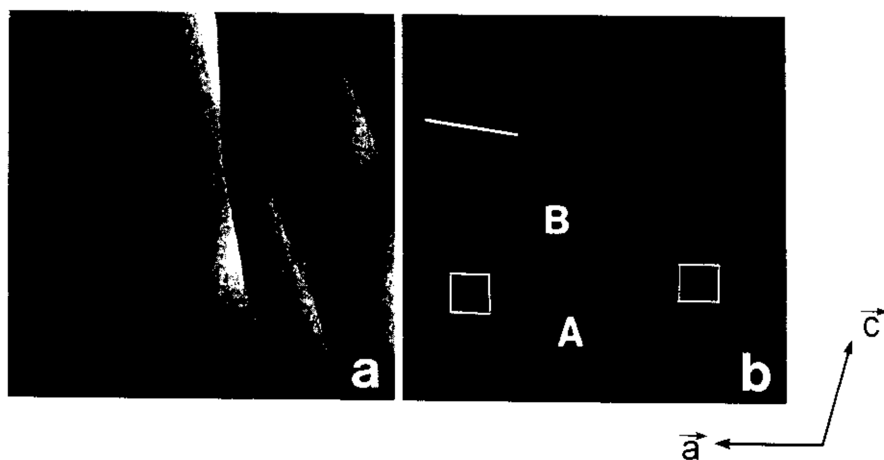

Fig. 2. a 35 × 35 μm² SFM topographical image of the (010) cleavage face of TGS. The height of the cleavage steps ranges from 1.2 to 5 nm. b FFM image of the same area. Frictional contrast *between* different domains marked by "A" and "B" is obvious. Additionally, frictional contrast *within* the domains can be observed. The line is parallel to the long axis of the positive domain

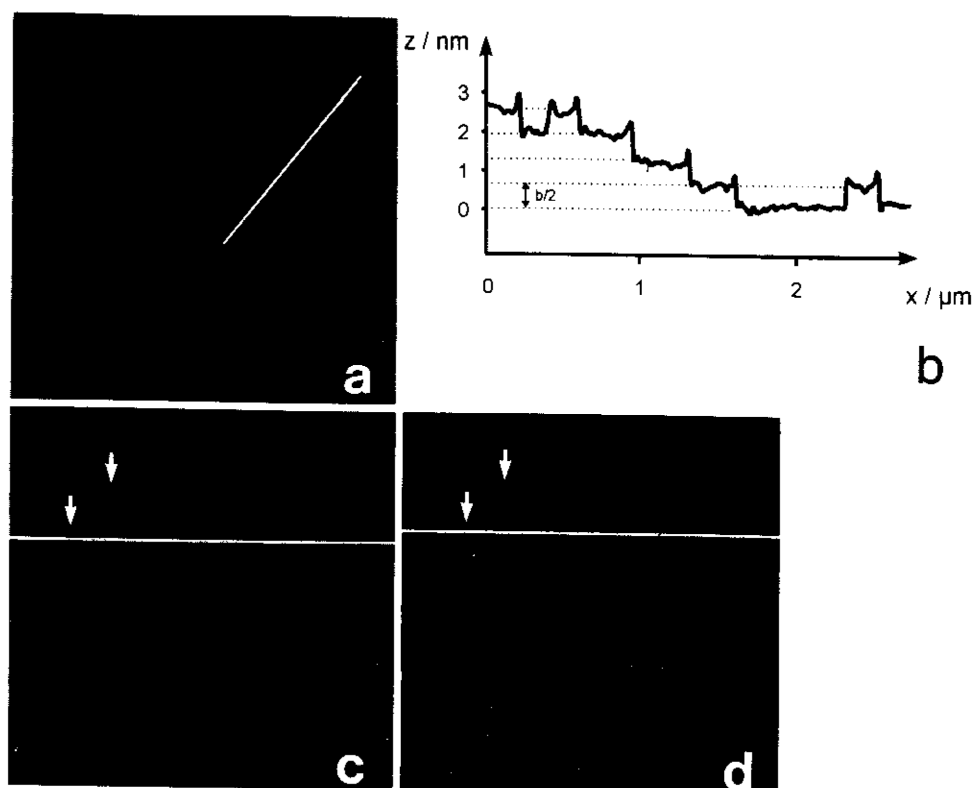

Fig. 3. **a** $5 \times 5\ \mu m^2$ topographical image of the surface of a positive domain. Terraces separated by steps with heights of $b/2$ are visible. The etch holes and islands also form steps with height $b/2$ to the surrounding terrace. **b** z-profile taken along the line indicated in **a**. The height differences of $b/2$ between the individual terraces are clearly visible. **c** Friction forward scan image of the same surface spot as in **a**. The comparison with the backward friction scan **d** shows a similar contrast behaviour for the terraces, holes, and islands. Only the frictional contrast of the step edges (see *arrows*) is reversed

polarity of ferroelectric domains in their SFM measurements. Additionally, it has been shown for Guanidinium Aluminium Sulfate Hexahydrate (GASH) crystals [31] that FFM is able to monitor the ferroelectric domain structure. A model of the contrast mechanism of ferroelectric domains in FFM is given elsewhere [32]. The silicon nitride tip has a permanent polarisation induced by trapped charges interacting with the electric field of the sample. This causes a twisting of the cantilever which gives an additional signal in the FFM image depending on the direction of the domain polarisation. Therefore, the regions marked by "A" and "B" in Fig. 2b can be attributed to domains of opposite polarity. Considering the differences in the etching behaviour mentioned above, area "A" is the surface of a negative and "B" the surface of a positive domain, respectively.

The long axis of the positive domain in Fig. 2b (see line) forms an angle of 10° with the sample a-axis. This behaviour is in good agreement with observations carried out with scanning electron microscopy [33] and optical microscopy [34] on TGS (010) surfaces where the long axis of lenticular domains was found to be inclined by about 12° to the [100] -direction towards the [001] -direction.

A closer look to the surface of a domain identified to be positive in the manner as described above is given in Fig. 3. The topography (Fig. 3a) reveals several terraces separated by steps with a height of half of the unit cell in b-direction. Moreover, several etch holes and two islands are visible separated also by steps of height $b/2$ from the surrounding terraces. The step structure is visualised in Fig. 3b by means of a z-profile taken along the line indicated in Fig. 3a.

The corresponding forward friction scan (i.e., the tip moving from left to right) is given in Fig. 3c. Two types of areas differing in their frictional behaviour are obvious, similar to those observed in Fig. 2b, where the positive domain was comprised of islands and etch holes also showing a different frictional contrast compared to the surrounding terrace. The comparison of the topographical map (Fig. 3a) with the friction image (Fig. 3c) shows that for terraces separated by heights of $n\,b$ ($n = 0, 1, 2, 3 \ldots$), the friction is always the same, whereas the frictional signal differs on terraces separated by heights of $n\,b + b/2$. Hence, frictional contrast occurs between different layers of the surface despite the homogeneous chemistry of the different terraces.

Comparison of the forward and backward (Fig. 3d) friction scan reveals an identical frictional contrast for the terraces, holes and islands for both scan directions, i.e., areas appearing dark in the forward friction scan appear also dark in the backward scan. The same happens with the bright contrast. This behaviour is contrary to conventional friction force measurements where the frictional contrast for the forward and backward scan direction is reversed (Fig. 4a) [27]. In this case, the contrast in the frictional signal is caused by differences in the chemical composition of the sample surface which modify the surface potential [35–37]. In the present case of TGS, however, an inhomogeneity of the chemical composition of the sample surface is very unlikely, since the topographical images show the typical cleavage structure of

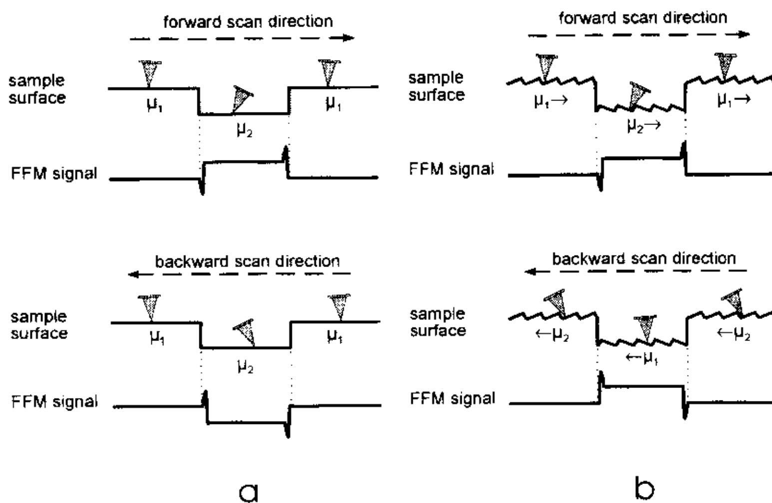

Fig. 4a, b. Principle of FFM contrast formation: **a** On materials which have no directional dependence of friction (i.e., the friction coefficient μ is the same in forward and backward scan direction), the contrast between surface areas exhibiting different μ is reversed when scanning forward compared to scanning in the backward direction since the FFM signal is a measure for the torsion of the cantilever. At the surface steps, peaks occur in the FFM signal due to some torque of the tip. **b** FFM tip probing the frictional force of a surface with asymmetric surface potential, illustrated by a saw-tooth like structure. The surface structure on the lower terrace is rotated by 180° along the surface normal compared to the structure on the upper terrace. The friction coefficient of one single terrace is, e.g., μ_1 in the forward scan direction, whereas it changes to μ_2 for the backward scan direction; ie., the friction coefficient is direction-dependent. The contrast recorded in the FFM signal is the same for both directions. The direction dependence, however, has no influence on the torque of the FFM tip at the surface steps

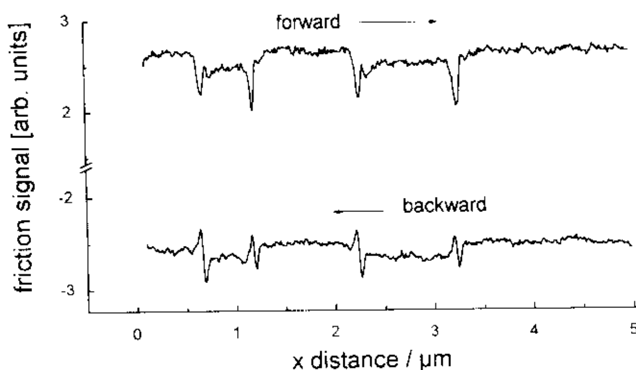

Fig. 5. Friction signal measured along the line drawn in Figs. 3c and d. The absolute value of the frictional forces varied about 3% between the individual terraces. The peaks in the forward and backward curve are caused by the torque of the cantilever at the step edges (Fig. 4)

a single-crystalline surface. Therefore, the identical frictional contrast for the forward and backward scan direction gives strong evidence for a dependence of the frictional forces on the scan direction, i.e., the frictional force on the tip is different when moved in forward or backward scan direction on an identical terrace (Fig. 4b).

This direction-dependent frictional contrast, however, should not have any influence on the expected torque of the cantilever at step edges which should be reversed for opposite scan directions as visible in Fig. 4. Comparison of Figs. 3c and d shows the predicted contrast reversal (arrows) for the forward and backward scan direction. The frictional signal acquired along the lines drawn in Figs. 3c and d is shown in Fig. 5 for both scan directions. The topographical steps causing the peaks in the curves are directed downward if looked from left to right in the diagram.

To confirm the directional dependence of the frictional contrast, the sample was rotated by different angles relative to the cantilever movement. A series of images for the negative domain is presented in Fig. 6 and for the positive domain in Fig. 7. For both positive and negative domains a characteristic surface spot was chosen (indicated by squares in Fig. 2b); sample and cantilever were arranged as presented in Fig. 8 and rotated by the angles as indicated. Only the forward scan direction of the cantilever is displayed, since the contrast observed when scanning forward or backward, is similar for all orientations as already shown in Fig. 3.

For a quantification of the frictional contrast, the difference in the frictional signals on the terraces separated by steps with height of $nb + b/2$ was calculated from profile lines taken from the FFM images. A reversed frictional contrast is expressed by an opposite sign of the contrast value.

The comparison of the FFM images for the negative domain at different sample rotation angles (Fig. 6) shows variations in both sign and magnitude of the frictional contrast on the terraces separated by steps of height $nb + b/2$. The frictional contrast is reversed for rotation angles α and $\alpha + 180°$. For the negative domain, the strongest contrast appears at $\alpha = 45°$ and 90°, respectively (and also at $\alpha = 225°$ and 270°, but with opposite sign), whereas it almost vanishes at $\alpha = 165°$. For the positive domain (Fig. 7), the frictional contrast is most prominent at $\alpha = 90°$ (and $\alpha = 270°$, with opposite sign), but in contrary to the negative domain, the frictional contrast vanishes at $\alpha = 0°$ and $\alpha = 180°$.

The magnitude of the frictional contrast between the areas exhibiting different frictional signals as a function of

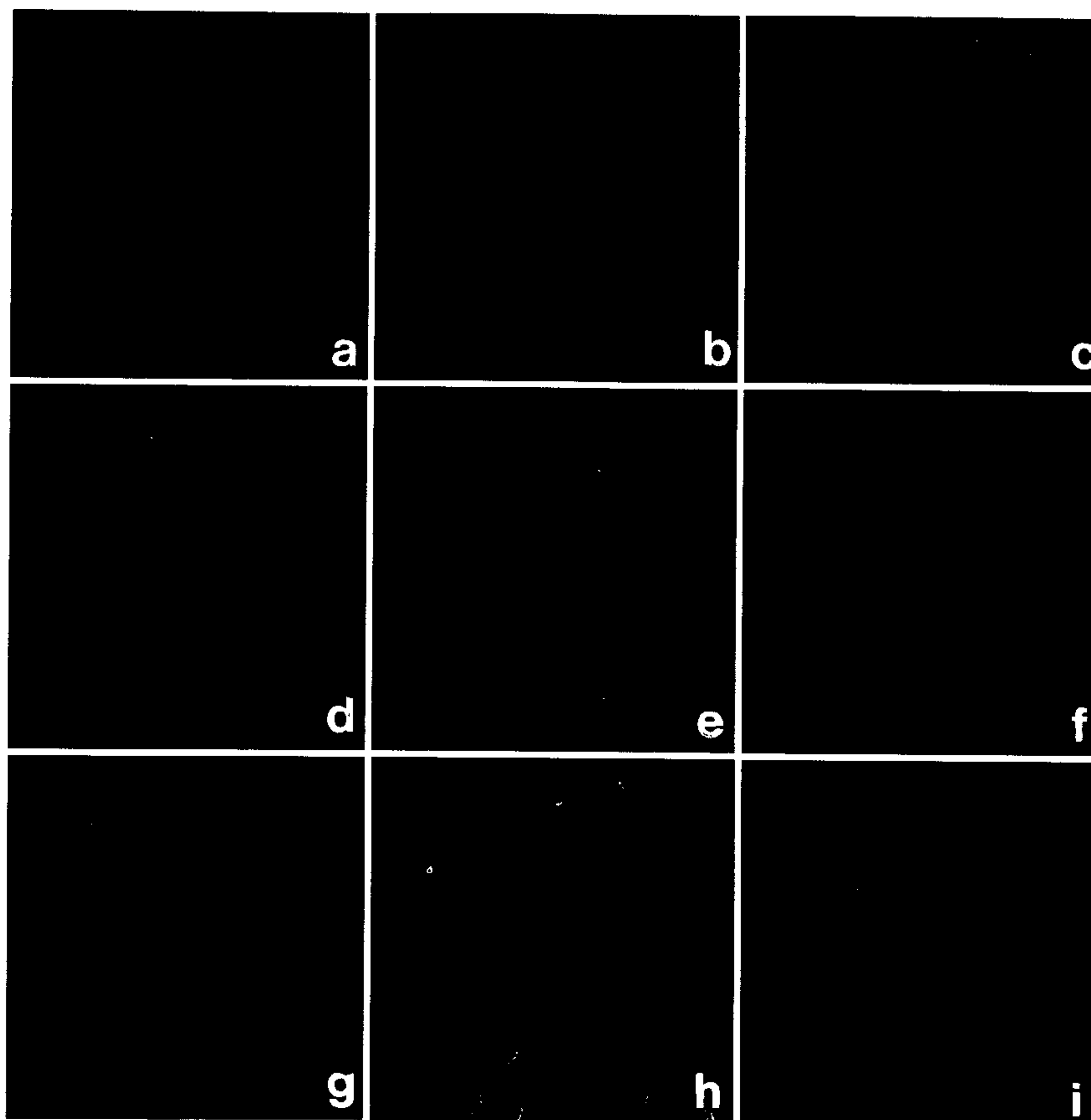

Fig. 6a–i. FFM images of a negative domain taken at the surface spot indicated in Fig. 2b. For the relative sample orientation and the cantilever scan direction see Fig. 8. The sample was successively rotated by angles of **a** 0°, **b** 45°, **c** 90°, **d** 135°, **e** 165°, **f** 180°, **g** 225°, **h** 270°, and **i** 315°. For all images the forward scan direction is shown

the sample rotation angle is presented in Fig. 9. The data points were calculated by averaging several profile lines taken from the friction force images. The diagram in Fig. 9 shows the difference in the friction force contrast for domains with different polarity already mentioned above. The contrast on the negative domain vanishes at about $\alpha = 165°$ and $345°$, whereas for the positive domain it disappears at $\alpha = 0°$ and $180°$. The magnitude of the maximum values for the frictional contrast on both domains is comparable and about 3% of the absolute value of the frictional forces.

Although care was taken during FFM imaging to maintain the same scan parameters (especially the loading force), deviations in the actual imaging conditions cannot be excluded due to, e.g., tip changes. Therefore, Fig. 9 shows only a rough qualitative dependence of the frictional contrast on the sample rotation angle. However, a phase shift in the frictional signals of the two domain types by approximately 15° is obvious. This observation gives evidence for a difference in the surface structure of the two domain types.

For the explanation of the directional-dependence and the anisotropy in the frictional contrast, a detailed examination of the crystal structure of TGS and the possible configurations of the (010) surface is necessary. Figure 1 shows the unit cell of the TGS structure drawn with the

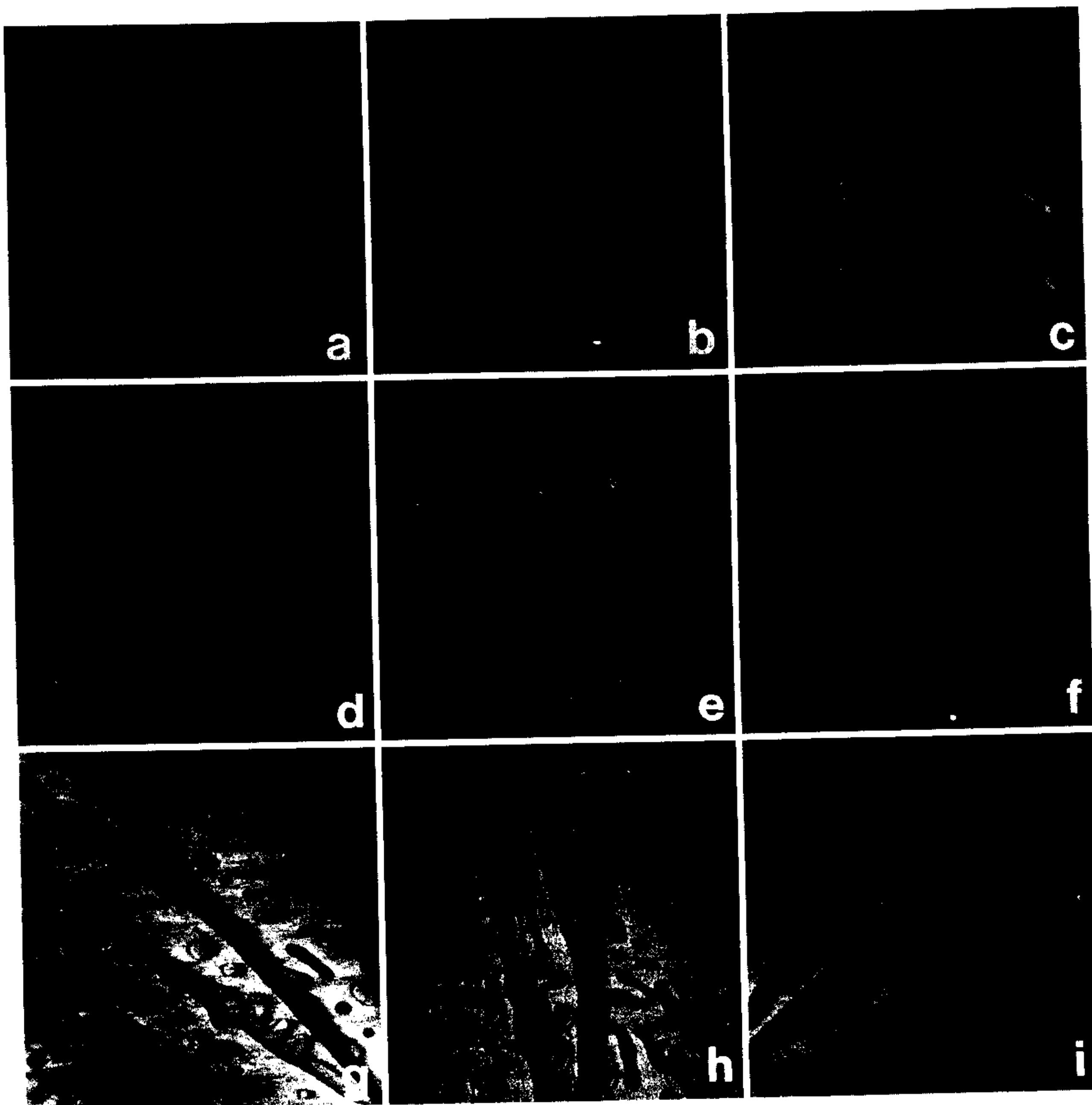

Fig. 7a–i. FFM images of a positive domain taken at the surface spot indicated in Fig. 2b. For the relative sample orientation and the cantilever scan direction see Fig. 8. The sample was successively rotated by angles of **a** 0°, **b** 45°, **c** 90°, **d** 135°, **e** 165°, **f** 180°, **g** 225°, **h** 270°, and **i** 315°. For all images the forward scan direction is shown

atom positions as determined by Hoshino et al. [38] and transformed to the crystal axes used in [19]. The transformation matrix was taken from [39].

The structure can be considered to consist of four different layers (depicted by A, A′, B, and B′ in Fig. 1) which have either a different chemical consistence or a different orientation. Both layers A and A′ contain SO_4-glycine 1 (G1) molecules, whereas B and B′ are built up from glycine 2 (G2)-glycine 3 (G3) molecules (the abbreviations and names for the glycine molecules are used as in [38]). Neighbouring layers have an average distance of $b/4$, closest layers of identical chemical composition are separated by $b/2$. Layers A and A′ are rotated against each other by a two-fold symmetry axis perpendicular to the layer surface (same for B and B′).

The topography of one single domain always and exclusively exhibits steps with height of $nb/2$ in SFM micrographs. Therefore, each domain possesses a surface with a homogeneous chemical composition. However, single terraces can show a different orientation of the molecular surface structure. Terraces separated by $nb + b/2$ have a surface structure rotated by 180° against each other.

From transmission electron microscopy measurements on TGS [40] it was already concluded that the positive and negative domains exhibit a different surface

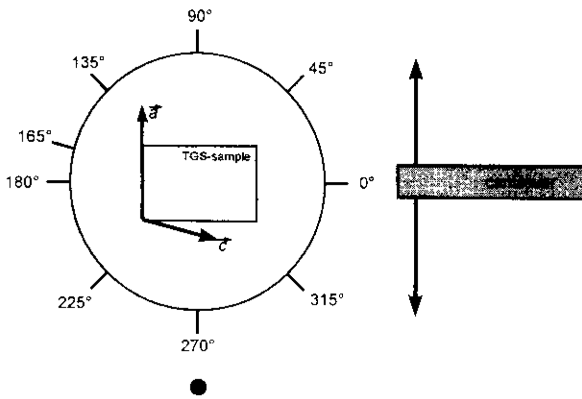

Fig. 8. Experimental arrangement of the measurements shown in Figs. 6 and 7. The orientation of the cantilever scan direction is fixed. The sample is mounted on a round sample holder with an accurate angle scale. The rotation angles given in Figs. 6 and 7 refer to that number which points to the *black dot* indicated in this figure. In the present case, the sample rotation angle would be denoted by 270°, and the cantilever (*right*) would scan parallel to the sample *a*-axis

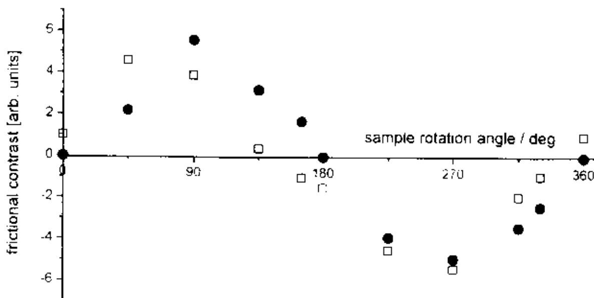

Fig. 9. Relative frictional contrast as a function of the sample rotation angle. A phase shift between the negative (□) and positive (●) domain by 15° can be observed

configuration. The experiments utilising a combination of the low-angle shadowing technique and the decoration technique revealed steps of height $b/4$ between neighbouring domains of opposite sign. The surface of the positive domains should always consist of SO_4-G1 layers (in our case layer A or A′), whereas the surface of the negative domains is composed of G2-G3 layers (B or B′). The arrangement of the molecules at the (010) surface for both domain types is shown in Figs. 10a and b.

From the knowledge of the symmetry relations between the different terraces on one domain it is possible to make a simple and intuitive approach to the phenomenon of the frictional contrast on TGS. As is shown in Fig. 5, the frictional signals for forward and backward scan directions are not reversed. This can only be explained by a different friction coefficient for the forward and backward scan direction on one single terrace, i.e., the friction coefficient on TGS (010) is not only *anisotropic*, but also *direction-dependent* according to the definitions in the introduction (Fig. 4). The difference in the friction coefficient should have its reason in the geometrical arrangement of the molecules on the surface which determines the surface potential and therefore the friction coefficient. Due to the 2_1 screw axis parallel to the *b*-direction, the terraces separated by steps of height $nb + b/2$ have a molecular surface structure rotated by 180° relative to each other. Hence, the friction coefficient on such a terrace must be the same for a tip moving in forward direction as the friction coefficient on a terrace with a rotated surface structure when moving the tip in backward direction.

A closer look to the molecular structure of the negative domain is given in Fig. 10a. The G2-G3 molecules form a saw-tooth-like structure perpendicular to the *c*-axis (Fig. 4b). From this structural model, the directional dependence of the friction behaviour for backward and forward scan direction can be expected to be strongest perpendicular to the *c*-axis since the anisotropy of the potential is most prominent in this direction. On the other hand, the directional dependence should be weakest along the *c*-axis. Comparing this assumption with the friction behaviour of the negative domain shown in Fig. 6, the observed frictional contrast can well be explained.

The friction behaviour can further be analysed in terms of the models for wearless friction already mentioned in the introduction. In most of these models, a stick-slip mechanism occurs caused by atoms or molecules jumping suddenly from one potential minimum to another, thereby dissipating energy. If the potential barrier between these minima looks different in forward or backward direction, the slip will occur at different points, and thus change the amount of the energy dissipated during the slip process. This leads directly to the observed difference in friction.

The molecular surface structure of the positive domain is displayed in Fig. 10b. The corrugation seems to be small in comparison to the surface of the negative domain. The most characteristic features are the oxygen atoms from the SO_4 molecules sticking out of the surface. They form rows along the *c*-axis. From the surface structure, the same friction behaviour as for the negative domain can be expected. Nevertheless, the frictional contrast vanishes not at scan directions parallel to the *c*-axis but at scan directions perpendicular to the *a*-axis. Hence, for the positive domain, the explanation of the friction contrast seems not to be as simple as for the negative domain and is still under investigation. It should, however, be noted at this point that, by measuring the frictional *contrast* between the terraces, the *difference* between the frictional force on different terraces is observed, not their absolute values.

In summary, it was shown that on (010) cleavage faces of ferroelectric TGS crystals, frictional contrast does not only occur between domains of different polarity, but also inside domains. Moreover, the frictional force was demonstrated to be highly anisotropic; the friction coefficient was even different when scanning forward compared to scanning backward in the same direction. This behaviour could be correlated with the crystallography of TGS which features an asymmetric arrangement of the molecules at the surface, thus causing an asymmetric surface potential which is traced by the FFM tip.

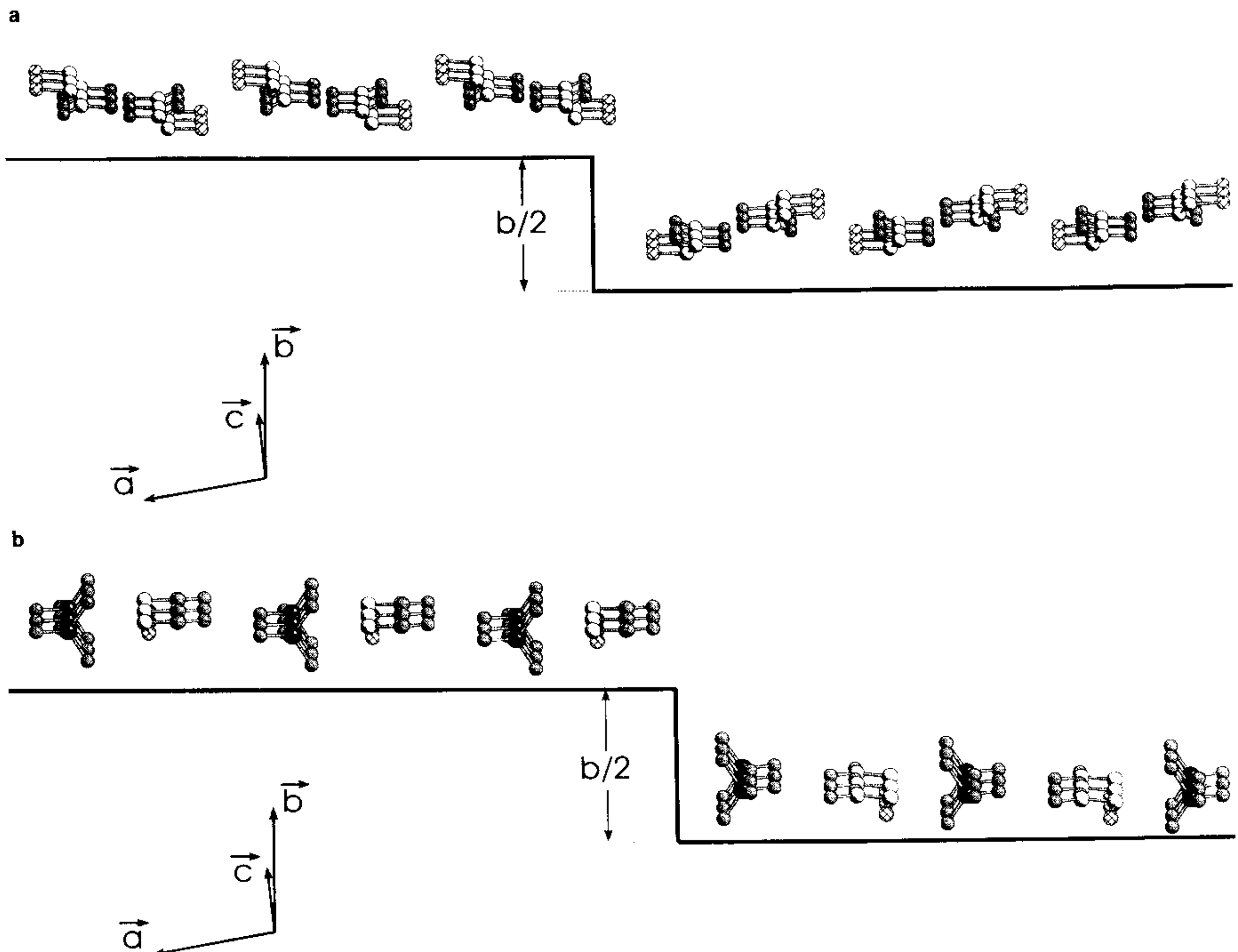

Fig. 10. **a** Perspective view of the (010) surface of a negative domain exhibiting a surface step of half of the unit-cell height. The structure consists of G2-G3 molecules forming a saw-tooth-like pattern perpendicular to the c-axis which is rotated by 180° around the b-axis on the lower terrace compared to the arrangement on the upper terrace. **b** The surface of the positive domain consisting of G1 SO_4 molecules. The characteristic features are the oxygen atoms sticking out of the surface and forming rows along the c-axis. The molecular arrangement on the lower terrace is again rotated by 180° compared to the upper terrace

Acknowledgements. We would like to thank L. Szczesniak from the Institute of Molecular Physics of the Polish Academy of Sciences for supplying the TGS samples. We are indebted to H.-K. Klaska, Institute of Mineralogy of the University of Hamburg for the determination of the crystal orientation by X-ray diffraction measurements. We also thank S. Pan, A. Schwarz and A. Wadas for helpful discussions. Financial support from the Deutsche Forschungsgemeinschaft (Grant No. Wi1277/2-1) is gratefully acknowledged.

References

1. B.J. Briscoe, D.C.B. Evans: Proc. R. Soc. London **A380**, 389 (1982)
2. C.M. Mate, G.M. McClelland, R. Erlandsson, S. Chiang: Phys. Rev. Lett. **59**, 1942 (1987)
3. G.A. Tomlinson: Philos. Mag. Ser. **7**, 905 (1929)
4. F.C. Frenkel, T. Kontorova: Zh. Eksp. Teor. Fiz. **8**, 1340 (1938) (Russian)
5. M. Hirano, K. Shinjo: Phys. Rev. **B 41**, 11837 (1990)
6. W. Zhong, D. Tománek: Phys. Rev. Lett. **64**, 3054 (1990)
7. D. Tománek, W. Zhong, H. Thomas: Europhys. Lett. **15**, 887 (1991)
8. G.M. McClelland, J.N. Glosli: In *Fundamentals of Friction: Macroscopic and Microscopic Processes*, ed. by I.L. Singer, H.M. Pollock, NATO ASI Seri E, Vol. 220 (Kluver, Dordrecht 1992) pp. 405–425
9. J.B. Sokoloff: J. Appl. Phys. **72**, 1262 (1992)
10. B.N.J. Persson: Phys. Rev. Lett. **71**, 1212 (1993)
11. J.A. Harrison, C.T. White, R.J. Colton, D.W. Brenner: Phys. Rev. B **46**, 9700 (1992)
12. J.A. Harrison, R.J. Colton, C.T. White, D.W. Brenner: Wear **168**, 127 (1993)
13. J.A. Harrison, C.T. White, R.J. Colton, D.W. Brenner: J. Phys. Chem. **97**, 6573 (1993)
14. Y. Enomoto, D. Tabor: Proc. R. Soc. A **373**, 405 (1981)
15. R. Takagi, Y. Tsuya: Wear **4**, 216 (1961)
16. Y. Tsuya: Wear **14**, 309 (1969)
17. M. Hirano, K. Shinjo, R. Kaneko, Y. Murata: Phys. Rev. Lett. **67**, 2642 (1991)
18. R.M. Overney, H. Takano, M. Fujihira, W. Paulus, H. Ringsdorf: Phys. Rev. Lett. **72**, 3546 (1994)

19. E.A. Wood, A.N. Holden: Acta Cryst. **10**, 145 (1957)
20. D. McKie, C. McKie: *Essentials of Crystallography* (Blackwell, Oxford 1986) pp. 250–261
21. Digital Instruments, Santa Barbara, CA, USA
22. O. Marti, J. Colchero, J. Mlynek: Nanotechnol. **1**, 141 (1990)
23. G. Meyer, N.M. Amer: Appl. Phys. Lett. **57**, 2089 (1990)
24. G.I. Distler, V.N. Lebedeva, E.V. Krasilnikova: Bull. Acad. Sci. USSR, Phys. Ser. **44**, 86 (1980) (in Russian)
25. U.D. Schwarz, H. Haefke, P. Reimann, H.-J. Güntherodt: J. Microsc. **173**, 183 (1994)
26. M. Labardi, M. Allegrini, M. Salerno, C. Frediani, C. Ascoli: Appl. Phys. A **59**, 3 (1994)
27. R. Overney, E. Meyer: Bull. Mater. Res. 26 (1993)
28. A. Sawada, R. Abe: Jpn. J. Appl. Phys. **6**, 699 (1967) and references therein
29. N. Nakatani: Jpn. J. Appl. Phys. **25**, 27 (1986)
30. H. Haefke, R. Lüthi, K.-P. Meyer, H.-J. Güntherodt. Ferroelectrics **151**, 143 (1994)
31. R. Lüthi, H. Haefke,, P. Grütter, H.-J. Güntherodt, L. Szczesniak, K.-P. Meyer: Surf. Sci. Lett. **285**, L498 (1993)
32. R. Lüthi, H. Haefke, K.-P. Meyer, E. Meyer, L. Howald, H.-J. Güntherodt: J. Appl. Phys. **74**, 7461 (1993)
33. K.-P. Meyer: Phys. Stat. Sol. (a) **94** K1 (1986)
34. A.G. Chynoweth, J.L. Abel: J. Appl. Phys. **30**, 1073 (1959)
35. R.M. Overney, E. Meyer, J. Frommer, D. Broadbeck, R. Lüthi, L. Howald, H.-J. Gütherodt, M. Fujihira, H. Takano, Y. Gotoh: Nature **359**, 133 (1992)
36. W. Allers, U.D. Schwarz, G. Gensterblum, R. Wiesendanger: Appl. Phys. A **59**, 11 (1994)
37. M. Labardi, M. Allegrini, F. Leccabue, B.E. Watts, C. Ascoli, C. Frediani: Solid State Commun. **91**, 59 (1994)
38. S. Hoshino, Y. Okaya, R. Pepinsky: Phys. Rev. **115**, 323 (1959)
39. B. Brezina, M. Havránková: Cryst. Res. Technol. **20**, 781 (1985)
40. N. Nakatani: Jpn. J. Appl. Phys. **18**, 491 (1979)

Appl. Phys. A 61, 357–362 (1995)

Applied Physics A Materials Science & Processing
© Springer-Verlag 1995

Scanning capacitance microscopy and spectroscopy applied to local charge modifications and characterization of nitride–oxide–silicon heterostructures

M. Dreyer, R. Wiesendanger

University of Hamburg, Institute of Applied Physics and Microstructure Research Center, Jungiusstrasse 11, D-20355 Hamburg, Germany (Fax: + 49-40/4123-6368)

Received: 10 March 1995/Accepted: 30 May 1995

Abstract. We have combined a home-built capacitance sensor with a commercial scanning force microscope to obtain a Scanning Capacitance Microscope (SCM). The SCM has been used to study Nitride–Oxide–Silicon (NOS) heterostructures which offer potential applications in charge storage technology. Charge writing and reading on a submicrometer scale is demonstrated with our SCM setup. In addition, SCM appears to be very useful for the characterization of subsurface defects in semiconductor devices which are inaccessible by most of the other scanning probe microscopies. Finally, we introduce a novel spectroscopic mode of SCM operation which offers combined voltage-dependent and spatially resolved information about inhomogeneous charge distributions in semiconductor devices.

PACS: 61.16.Ch; 73.40.Qv; 73.90. + f; 68.35.Bs

Spatially resolved capacitance measurements by means of a sharp metal probe being scanned in close proximity to a sample [1] appear to be highly promising for the characterization of dielectric thin films and semiconductor devices on a submicrometer length scale.

With the advent of scanning probe technology [2, 3], Scanning Capacitance Microscopes (SCM) [4–10] have usually been realized by a combination of an Atomic Force Microscope (AFM) [11] with a commercial RCA [12] or a home-built capacitance sensor. Interesting applications of SCM were found in the near-field lateral dopant profiling of semiconductor devices [5] and charge storage in Nitride-Oxide Silicon (NOS) heterostructures [6–8] on a submicrometer scale. Another interesting potential application of the SCM would be high-resolution capacitance spectroscopy at low temperatures [13]. Here, we report on the design of a novel simple home-built capacitance sensor which has been combined with a commercial scanning probe instrument [14] to obtain a SCM. We have applied the SCM to study NOS heterostructures with varying oxide thickness. Subsurface defects have been imaged with submicron spatial resolution which did not show up in topographic AFM maps. By applying voltage pulses between the SCM tip and the NOS structures, we succeeded in charge storage on a submicrometer length scale. The stored charge bits have been studied as a function of the applied bias voltage. Spatially resolved spectroscopic SCM studies are presented for the first time which are very useful to understand the SCM image contrast.

1 Experimental

NOS heterostructures have been selected as samples because they provide interesting model systems for charge storage [15], leading to a spatially varying capacitance signal as measured by means of a sharp metal probe being scanned in close proximity to the top nitride layer. Three different samples have been prepared. The substrates of the NOS heterostructures consisted of p-doped Si(100) wafers with a resistivity of 10–20 mΩ cm, on which a tunnel oxide of varying thickness (5.1, 6.6, and 8.2 nm) has been grown. Finally, a 52–53 nm thick nitride layer has been deposited on top.

If a metal electrode is brought in contact with the top nitride layer of the NOS heterostructure (Fig. 1), a Metal-Insulator-Silicon (MIS) diode is formed. In the following, we will discuss the capacitance C of the MIS diode as a function of the bias voltage U applied to the silicon substrate. This voltage is partially dropped across the Insulator (I), consisting of the nitride and the oxide layers, and partially across the depletion layer at the insulator-silicon interface. The total capacitance of the MIS-diode C_{MIS} consists therefore of a series of the insulator's capacitance C_I and the capacitance of the depletion layer C_D, and one finds:

$$C_{MIS} = \frac{C_I C_D}{C_I + C_D}. \quad (1)$$

The capacitance of the insulating layer of thickness d and effective cross section area A (being identical with the

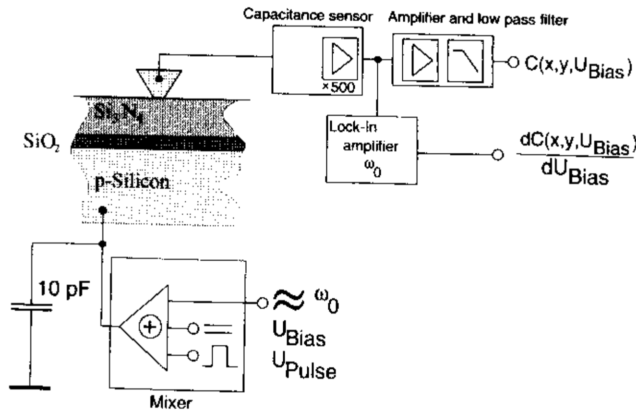

Fig. 1. Schematic drawing of the NOS heterostructure in contact with a metal probe tip and the capacitance detection circuitry

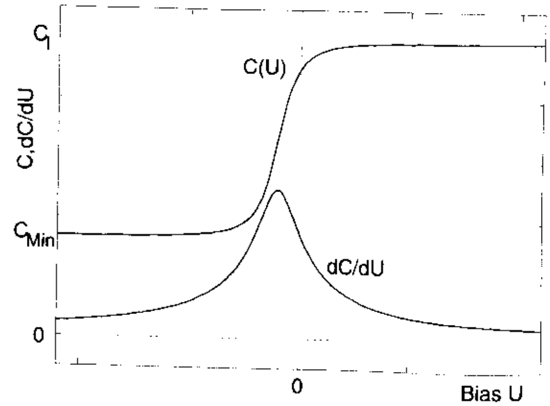

Fig. 2. Schematic drawing of the dependence of the capacitance C on the applied bias voltage U for an ideal MIS diode. In addition, the voltage-dependence of the first derivative dC/dU is shown

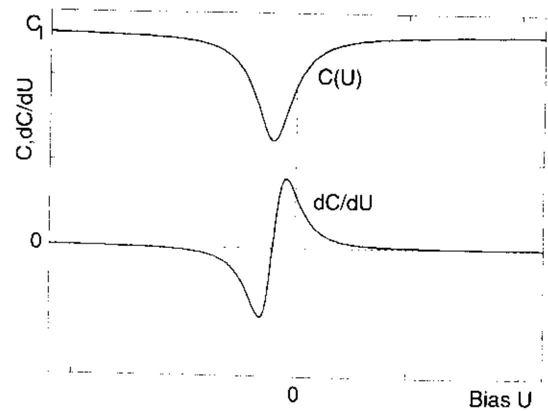

Fig. 3. Schematic drawing of the dependence of the capacitance C and the first derivative dC/dU on the applied bias voltage U for a real MIS diode

contact area of the top metal electrode) is:

$$C_I = \varepsilon_I \frac{A}{d}, \tag{2}$$

where ε_I denotes the dielectric constant of the insulator, which is assumed to be equal for the nitride and the oxide layer to a first approximation. The capacitance of the depletion layer is

$$C_D = \varepsilon_{Si} \frac{A}{w}, \tag{3}$$

where w denotes the width of the depletion zone. Since this width w depends on the externally applied bias voltage U, the total capacitance C_{MIS} of the MIS diode becomes voltage-dependent.

For a p-doped silicon substrate and a positive applied bias voltage, no depletion zone exists and the total capacitance C_{MIS} is equal to C_I (Fig. 2). On the other hand, in the case of negative applied bias voltage, a depletion zone builds up until inversion is reached and the depletion layer ceases to grow. This corresponds to the minimum value of C_D and therefore C_{MIS} as well (Fig. 2). For a real MIS diode, recombination effects have to be considered as well. If the applied voltage over the MIS diode is swept with a rate on the order of the generation recombination rate or smaller, a carrier exchange between the depletion zone and the inversion layer takes place. Consequently, the electron concentration can follow the external bias voltage in the case of strong inversion. Therefore, the total capacitance C_{MIS} tends towards C_I in the limit of high negative applied bias voltage as well, which results in a $C_{MIS}(U)$ dependence as shown in Fig. 3.

NOS heterostructures have been considered as charge storage devices for a long time [15]: By applying a voltage pulse between the top metal electrode and the silicon substrate, electrons can tunnel through the oxide layer leaving holes behind. This charge carrier separation leads to an additional electrical voltage across the NOS structure and can be detected capacitively by measuring C or dC/dU at an appropriate fixed value of the external applied bias voltage, as shown below. Depending on the oxide thickness, which should be not too small and homogeneous, the separated charge remains stable for many years. By applying a voltage pulse of opposite polarity, however, the stored charge can be erased which is an attractive feature for memory applications.

If the top electrode is a metallized sharp probe tip as used for AFM, ultra-high density storage devices may be realized [6, 7]. Read-out is achieved by combining a capacitance sensor with a standard AFM instrument to obtain a SCM. Assuming a contact area of $A = 1\ \mu m^2$ and a thickness of the insulating layer of $d = 55$ nm, the capacitance C_I is on the order of 1 fF. If the contact area is further reduced to the nanometer-scale regime, C_I is only on the order of aF (10^{-18}F). In previous works [6–8], a commercial capacitance sensor from RCA [12] with a sensitivity of 100 mV/fF was used. In the present work, we have developed our own capacitance sensor which is based on a simple concept. It basically consists of a resonance circuitry with an inductance L, a capacitance $C = C_{MIS} + C_P$, where C_{MIS} is the capacitance of the MIS diode to be measured and C_P is a parasitic capacitance, and a parasitic resistance R. The resonance circuit is driven by an external sinusoidal signal of frequency ω_{ext}. The amplitude and phase of the driven oscillation depends

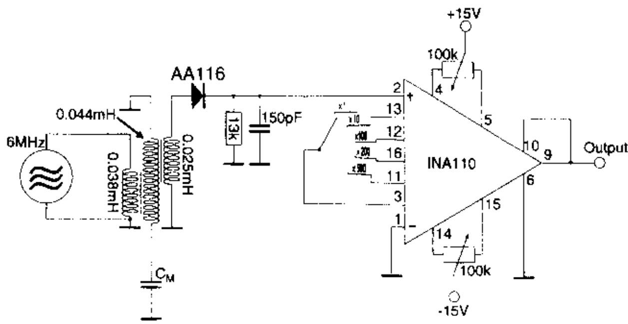

Fig. 4. Schematics of our home-built capacitance sensor

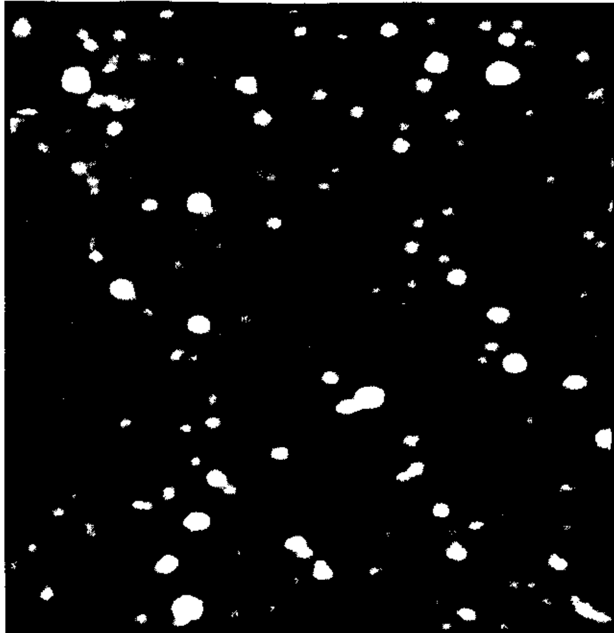

Fig. 5. AFM image ($1 \times 1\ \mu m^2$) showing the surface topography of the top nitride layer of the NOS heterostructure. Total grey scale: 5.8 nm; rms-roughness: 0.5 nm

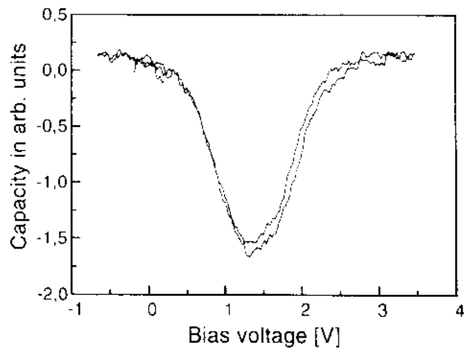

Fig. 6. Typical $C(U)$ characteristic as measured for the tungsten-tip nitride oxide silicon diode

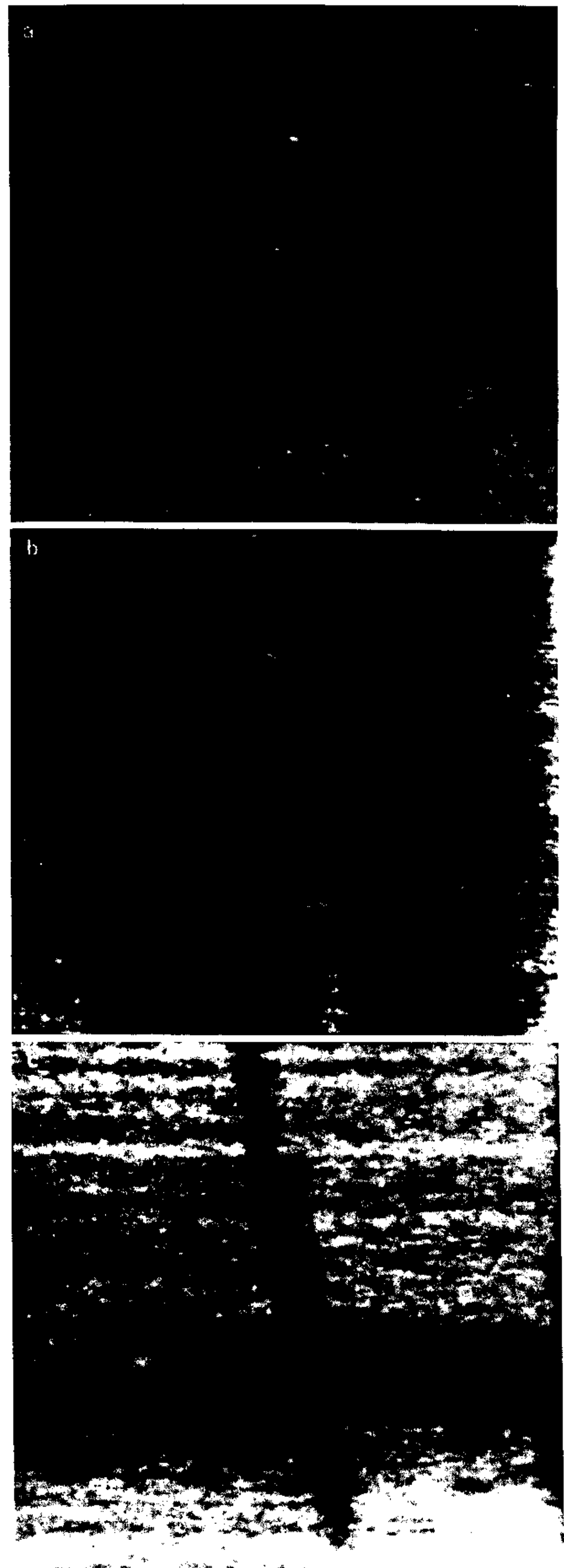

Fig. 7a–c. Simultaneously recorded topographic **(a)** capacitance **(b)**, and dC/dU image **(c)** of the same area ($35 \times 35\ \mu m^2$) of a NOS heterostructure sample. A subsurface defect shows up in the C and dC/dU images but remains invisible in the surface topographic image

on the difference between the driving frequency ω_{ext} and the resonance frequency ω_{res} which itself depends on the capacitance C_{MIS} to be measured. Therefore, the capacitance sensor can be based on either amplitude or phase detection. The schematic drawing of our capacitance sensor, based on amplitude detection, is shown in Fig. 4. We achieved a sensitivity of 15 mV/fF with a gain factor of 500, while the noise level was on the order of 5 mV. This capacitance sensor has finally been connected with a commercial AFM [14].

2 Results and discussion

We have first used AFM to characterize the surface topography of the top nitride layer. Figure 5 shows an AFM map ($1 \times 1\ \mu m^2$) obtained with an ultra-sharp 'contamination' tip. The total grey scale corresponds to a height difference of 5.8 nm over the whole image. The rms-roughness is as small as 0.5 nm which demonstrates that the surfaces are reasonably flat for nanometer-scale storage applications.

For capacitance measurements, we have initially used home-made tungsten cantilevers cut from 5 µm thick tungsten foil and electrochemically etched to obtain sharp probe tips. The front end of these cantilevers were bent mechanically so that the tip end could easily be brought in contact with the NOS heterostructure without having large tilt angles. The contact area was chosen not to be too small in order to obtain reasonable signal-to-noise ratio for the measured capacitance signal.

A typical $C(U)$ characteristic of the tungsten-tip nitride–oxide–silicon diode is presented in Fig. 6. The dependence of the measured capacitance C on the applied bias voltage U is in agreement with theoretical expectation (Fig. 3).

As a next step, we have combined the capacitance detection with spatially resolved measurements by scanning

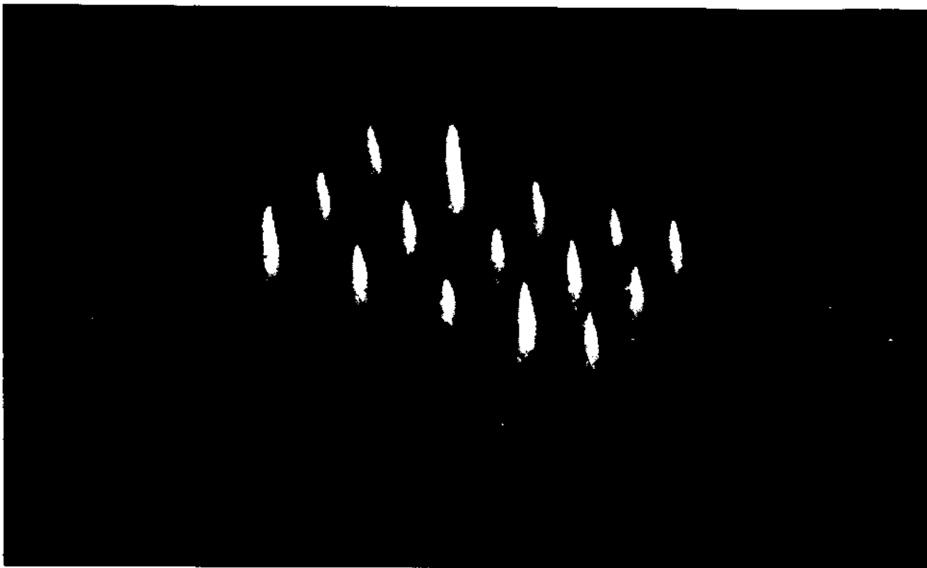

Fig. 8. Perspective dC/dU-image ($15 \times 15\ \mu m^2$) of a 5×3 array of charge bits which were written by applying -35V pulses of 40 µs width between the metal tip and the silicon substrate of the NOS heterostructure with an oxide thickness of 5.1 nm. No features appeared in the corresponding topographic image

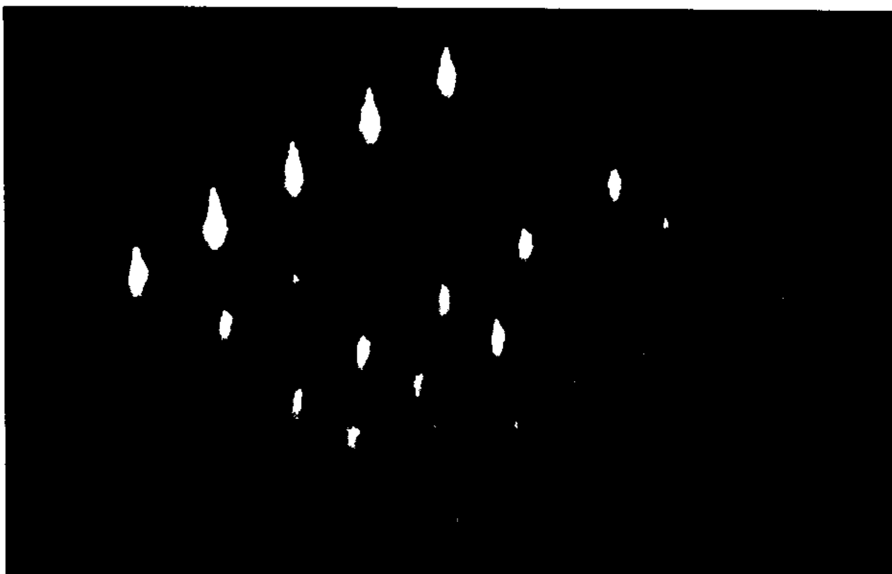

Fig. 9. Perspective dC/dU image of an array of charge bits which were written with voltage pulses of variable height and width. *Upper two rows*: pulse height of -38 V, pulse width varied between 100 and 20 µs; *lower two rows*: pulse height of -35 V, pulse width varied between 100 and 40 µs. For this series of charge modifications the NOS heterostructure with an oxide thickness of 6.6 nm has been used

the NOS sample relative to the metal probe tip. Three signals were recorded simultaneously as a function of lateral (x, y)-position:

(*i*) the topographic (z) signal of normal contact AFM operation,
(*ii*) the capacitance (C) signal, and
(*iii*) the first derivative (dC/dU) signal by using lock-in detection (Fig. 1).

An example is presented in Fig. 7 where we have succeeded in locating a subsurface defect which is easily recognizable in the capacitance and dC/dU images but does not show up in the corresponding topographic image. Such defects, which probably result from inhomogeneities at the oxide–silicon interface, were extremely rare in our samples. However, the present example demonstrates nicely the potential of SCM for imaging and characterization of subsurface defects with submicron spatial resolution which do not show up at the surface and therefore remain invisible for most other scanning probe microscopies.

By applying voltage pulses between the metal tip and the silicon substrate, we succeeded in charge separation by tunneling through the oxide layer as described in Sect. 1. The patterns of stored charge bits have subsequently been imaged with the SCM. An example is presented in Fig. 8, where a 5×3 array of charge bits is visible which was written with -35V pulses of 40 µs width. The size of the written charge bits, as they appear in the SCM images, depends mainly on three parameters:

1) The contact area between the metal tip and the NOS heterostructure which determines the degree of charge localization during the writing process as well as the contour profile of the charge bits during the SCM imaging (read-out) process.
2) The parameters for the voltage pulses (height and width) which determine how much charge can actually tunnel through the oxide layer. Figure 9 shows a series of charge bits written with variable pulse parameters, but with the same SCM tip. The size of the charge bits varies considerably.
3) The chosen value of the applied bias voltage during SCM imaging which has also great influence on the apparent size of the charge bits, as will be discussed below.

To extract more information about the characteristics of the stored charge bits, we have performed Scanning Capacitance Spectroscopy (SCS) studies, i.e., we have investigated the bias-dependence of the dC/dU signal as a function of the spatial coordinates (x, y). In Fig. 10, we present SCS data ($dC/dU\,[x, U]$) measured over three previously written charge dots. The data are shown in a top-view (Fig. 10a) as well as in a perspective view (Fig. 10b). The information content of such maps is extremely high because both the spatial as well as the bias-dependence of the dC/dU signal is presented simultaneously. To discuss the information content of this data, it is therefore advantageous to plot section lines at fixed spatial coordinate (Fig. 11a) or at fixed bias voltage (Fig. 11b) separately.

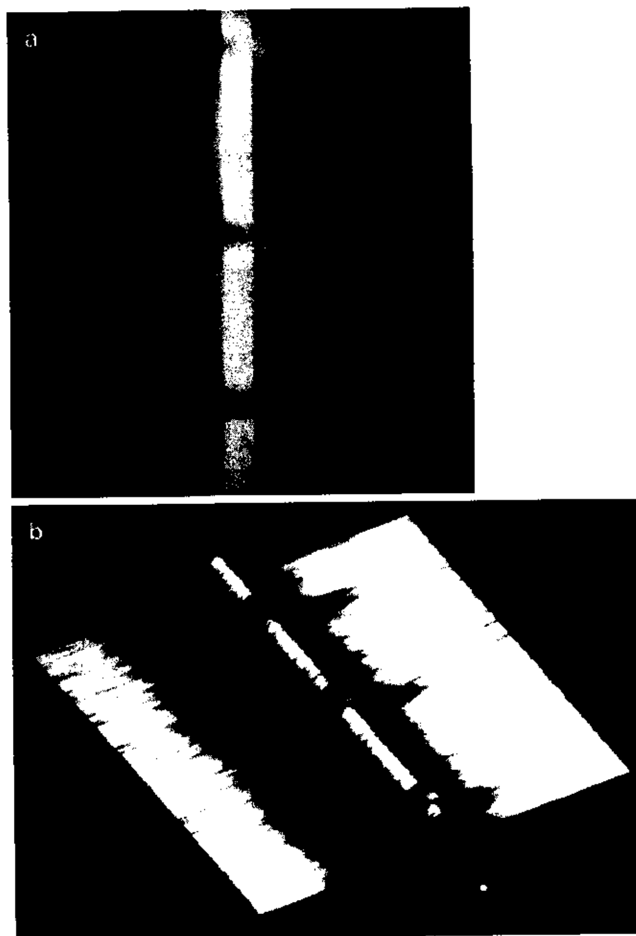

Fig. 10. **a** Top-view of a SCS (dC/dU) image of three previously written charge dots (pulse height: -35 V, pulse widths: 100, 80 and 60 µs from *bottom to top*). The applied bias voltage has been varied along the *horizontal axis* whereas the *vertical axis* represents the spatial (x-) coordinate. **b** Perspective view of the same spectroscopic SCM data as presented in **(a)**

Figure 11a shows $dC/dU(U)$ characteristics at several different x-locations. The shape of these curves agree with the theoretical expectation (Fig. 3). More interestingly, the $dC/dU(U)$ characteristic above a written charge dot appears to be shifted and flattened compared to a $dC/dU(U)$ curve above a non-modified sample location. The shift along the voltage axis corresponds to an additional local voltage which originates from the separated charge in the NOS heterostructure as already described in the experimental part. The sign of this voltage shift depends on the sign of the applied voltage pulses which has been verified experimentally. In Fig. 11b, we present $dC/dU(x)$ curves for several different values of the applied bias voltage U. It is obvious that the apparent size of the charge dots, as imaged with the SCM, depends critically on the chosen U value. Therefore, it is not useful to provide numbers for the size of the written charge bits without specifying the bias voltage used for imaging (read-out). If the applied bias voltage is chosen too high, the written charge dots are not showing up at all in the dC/dU image.

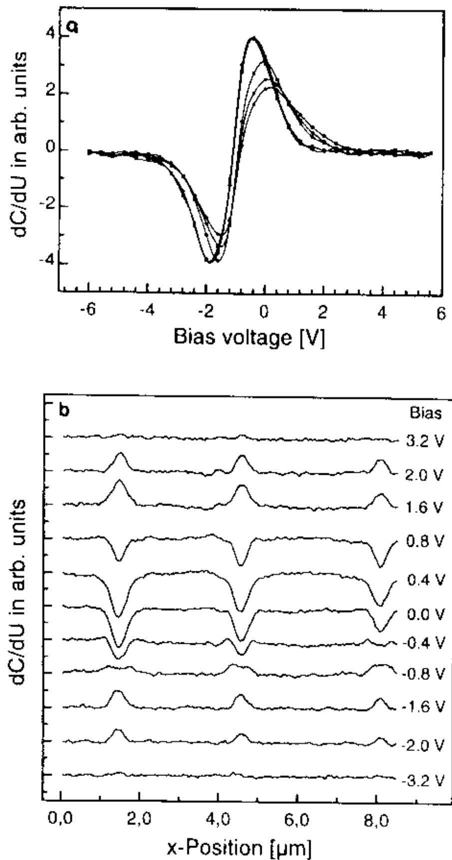

Fig. 11. a Individual section lines across the data shown in Fig. 10 at several different values of (fixed) x-position. **b** Individual section lines across the data shown in Fig. 10 at several different values of (fixed) bias voltage U

3 Summary and conclusions

We have combined a home-built capacitance sensor with a commercial AFM to obtain a SCM. The SCM has been used to study NOS heterostructures at submicron spatial resolution. We were able to image subsurface defects which did not show up in the corresponding surface topographic image. The C–U and dC/dU–U characteristics as measured locally with the SCM were found to be in agreement with theoretical expectations. By applying voltage pulses between the metallic SCM tip and the silicon substrate, charge dots have successfully been written on a submicron length scale. These charge dots have subsequently been analyzed by SCS. Future work will focus on improvements in the sensitivity of the capacitance sensor which will allow to study much smaller contacts between the metal tip and the NOS heterostructure.

Acknowledgements. We would like to thank Ch. Wobbe and Dr. S. Pan for useful discussions, and N. Bündgens and Dr. Cortes from Philips Semiconductors, Hamburg, for providing the NOS samples. Financial support by the Bundesministerium für Forschung und Technologie (grant No. 13N6276) is gratefully acknowledged.

References

1. J.R. Matey, J. Blanc: J. Appl. Phys. **57**, 1437 (1985)
2. G. Binnig, H. Rohrer: Helv. Phys. Acta **55**, 726 (1982)
3. R. Wiesendanger: *Scanning Probe Microscopy and Spectroscopy: Methods and Applications* (Cambridge Univ. Press, Cambridge 1994) pp. 279
   R. Wiesendanger, H.-J. Güntherodt (eds.): *Scanning Tunneling Microscopy II*, 2nd edn., Springer Ser. Surf. Sci., Vol. 28 (Springer, Berlin, Heidelberg 1995)
4. C.C. Williams, W.P. Hough, S.A. Rishton: Appl. Phys. Lett. **55**, 203 (1989)
5. C.C. Williams, J. Slinkman, W.P. Hough, H.K. Wickramasinghe: Appl. Phys. Lett. **55**, 1662 (1989)
6. R.C. Barrett, C.F. Quate: J. Appl. Phys. **70**, 2725 (1991)
7. R.C. Barrett, C.F. Quate: Ultramicrosc. **42–44**, 262 (1992)
8. B.D. Terris, R.C. Barrett, H.J. Mamin: SPIE Proc. **1855**, 195 (1993)
9. Y. Huang, C.C. Williams: J. Vac. Sci. Technol. B **12**, 369 (1994)
10. Š. Lányi, J. Török, P. Rehurek: Rev. Sci. Instrum. **65**, 2258 (1994)
11. G. Binnig, C.F. Quate, Ch. Gerber: Phys. Rev. Lett. **56**, 930 (1986)
12. R.C. Palmer, F.J. Denlinger, H. Kawamoto: RCA Rev. **43**, 194 (1982)
13. R.C. Ashoori, H.L. Stormer, J.S. Weiner, L.N. Pfeiffer, S.J. Pearton, K.W. Baldwin, K.W. West: Phys. Rev. Lett. **68**, 3088 (1992)
14. TMX 2000, Topometrix
15. S. Iwamura, Y. Nishida, K. Hashimoto: IEEE Trans. ED-**28**, 854 (1981)